

Effect of intermetallic phases on the anodic oxidation and corrosion of 5A06 aluminum alloy

Song-mei Li, Ying-dong Li, You Zhang, Jian-hua Liu, and Mei Yu

School of Materials Science and Engineering, Beihang University, Beijing 100191, China
(Received: 23 June 2014; revised: 16 August 2014; accepted: 25 August 2014)

Abstract: Intermetallic phases were found to influence the anodic oxidation and corrosion behavior of 5A06 aluminum alloy. Scattered intermetallic particles were examined by scanning electron microscopy (SEM) and energy dispersive spectroscopy (EDS) after pretreatment. The anodic film was investigated by transmission electron microscopy (TEM), and its corrosion resistance was analyzed by electrochemical impedance spectroscopy (EIS) and Tafel polarization in NaCl solution. The results show that the size of Al–Fe–Mg–Mn particles gradually decreases with the iron content. During anodizing, these intermetallic particles are gradually dissolved, leading to the complex porosity in the anodic film beneath the particles. After anodizing, the residual particles are mainly silicon-containing phases, which are embedded in the anodic film. Electrochemical measurements indicate that the porous anodic film layer is easily penetrated, and the barrier plays a dominant role in the overall protection. Meanwhile, self-healing behavior is observed during the long immersion time.

Keywords: aluminum alloys; intermetallic particles; anodic oxidation; corrosion; protective films

1. Introduction

Aluminum 5A06 alloy is widely used for many applications in marine and construction industries due to its high strength-to-weight ratio [1]. The presence of intermetallic precipitation in the alloy matrix improves the mechanical properties of the alloy but leads to a higher susceptibility to local corrosion [2–3] since the second phase particles are usually preferred sites of cathodic or anodic activity [4]. Severe localized attack always occurs due to the galvanic coupling between the active intermetallic phases and the nobler aluminum alloy matrix. For example, β -phase (Al_3Mg_2) has a corrosion potential of about -1.29 V vs. saturated calomel electrode (SCE), compared with -0.73 V vs. SCE for the matrix, which implies the increased anodic activity towards dissolution in a corrosive environment [5]. Mg–Si phase (Mg_2Si) has the similar or lower values of corrosion potential relative to the surrounding matrix [6]. The investigation of local corrosion behavior of solid solution aluminum alloys (e.g., Al–Cu, Al–Mg, and Al–Si) has received considerable attention [7–9]. Some reports also fo-

cus on the influence of specialized intermetallics on the anodic behavior of aluminum alloys [10–14]. Generally, anodizing is an electrochemical process that consists of converting aluminum or its alloys into oxides by an appropriate selection of the electrolyte and the anodizing conditions such as applied potential, duration, and current density. However, additional effects are evident in the anodizing of aluminum alloys containing complex intermetallics; these effects depend on the composition, shape, size, and volume fraction of the inclusions. The alloy intermetallics influence the film structure as well as the corrosion resistance. It is crucial to understand the relative contributions of the solid solution matrix and intermetallics to the film behavior and, hence, to further optimize the anodizing process for practical applications.

In this work, intermetallics in commercial 5A06 aluminum alloy were studied before and after the anodizing process. Transmission electron microscopy (TEM) and scanning electron microscopy (SEM) were used to elucidate the effects of intermetallic particles on the film formation process. Electrochemical measurements, including electrochemical

impedance spectroscopy (EIS) and Tafel polarization, were employed to provide a comprehensive understanding of the corrosion resistance of the prepared anodic films.

2. Experimental

Aluminum 5A06 alloy samples (nominal composition: Mg 5.8wt%–6.8 wt%, Mn 0.5wt%–0.8wt%, Fe 0.4wt%, Si 0.4wt%, Cu 0.1wt%) with dimensions of 100 mm × 50 mm × 2 mm were etched in 50 g·L⁻¹ NaOH solution at 50°C for 1 min and then desmutted in 300 g·L⁻¹ HNO₃ for 1 min at room temperature. A two-electrode configuration with a 5A06 aluminum alloy plate as the anode and a stainless plate as the cathode was employed for anodizing. The anodizing bath contained 50 g·L⁻¹ sulfuric acid and 10 g·L⁻¹ adipic acid. A constant voltage of 15 V was applied, and the anodizing time was 20 min. The temperature was maintained at (25 ± 0.5)°C under vigorous stirring. After anodizing, the samples were rinsed in deionized water. Hydrothermal sealing was carried out in boiling water for 30 min.

The surface morphology was examined by field-emission scanning electron microscopy (FE-SEM; Hitachi S-4800), and the chemical composition was investigated by energy dispersive spectroscopy (EDS). Cross sections were prepared with a nominal thickness of 20 nm using an ion thinner beam and then examined by transmission electron microscopy (TEM; JEM-2100F).

The electrochemical behaviors of the anodized samples were examined by electrochemical impedance spectroscopy (EIS) and Tafel polarization in a 3.5wt% NaCl solution using a conventional three-electrode cell with a saturated calomel electrode (SCE) as the reference electrode, a platinum plate as the counter electrode, and the anodized sample as the working electrode (exposed area of 1 cm²). EIS measurements were conducted at open circuit potential (E_{OCP}) by applying a 10-mV sinusoidal perturbation in a 10⁵–10⁻² Hz frequency range with seven experimental points per frequency decade presented by Bode plots. Tafel polarization was conducted from -250 mV to 250 mV vs. E_{OCP} using a scan rate of 0.17 mV·s⁻¹.

3. Results and discussion

3.1. Alloy intermetallic phases

Fig. 1 shows the morphology of 5A06 aluminum alloy after etching and desmutting, and Fig. 2 displays the SEM micrographs of 5A06 aluminum alloy after anodizing. Different zones in these micrographs were analyzed by EDS to determine the typical intermetallic types, and the results are

listed in Table 1. Preferential dissolution causes the dealloying of intermetallics, which enriches the surface in iron, magnesium, and manganese, as shown in Table 1. The main types of observed intermetallic particles are (Fe, Al, Mn, and Mg)-containing intermetallics, which are represented by several phases including Al₆(Fe,Mn), Al₃Mg₂, and Al₆Mn. Two different types of intermetallics are present within the examined area: one is enriched in iron (1#–7#), while the other is free of iron (10#–13#). Particles that are several microns in size (1#–4#) exhibit the relatively high element ratios of iron, whereas smaller particles (5#–7#) contain the same types of elements but are depleted in iron. No iron is detected on the submicron particles (10#–13#). In other words, large particles are mainly enriched in iron, and the particle size tends to decrease with iron content. Some holes are observed on the surface, probably due to the removal of intermetallics from the matrix during pretreatment. The alloy matrix is mainly composed of Al and Mg (7# and 8#), indicating the dominant role of β-phase (Al₃Mg₂) in the matrix. Silicon-containing particles fail to be detected and are probably totally removed by the pretreatment procedure.

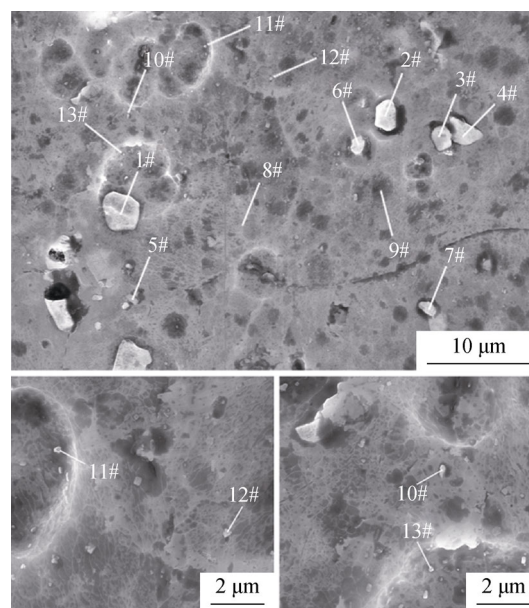


Fig. 1. SEM micrograph of a 5A06 aluminum alloy surface after etching and desmutting.

3.2. Morphology of the anodic film

Fig. 2 displays the SEM micrographs of 5A06 aluminum alloy after anodizing. Anodizing causes drastic changes in the surface morphology. In comparison with the original morphology, the most obvious difference is the decrease of visible particles. Most intermetallics tend to dissolve during the anodizing process. The anodic film is integral, and the main defects are focused on the positions of removed inter-

metallics, leaving shallow craters. The detailed structure of the anodic film is revealed by amplifying the local flat area in Fig. 2(b). The film is porous with regular pore size, and the inhomogeneous appearance is probably attributed to the influence of intermetallics. The chemical compositions of test areas marked in Figs. 2(c) and (d) are listed in Table 1.

Magnesium is hardly detected (16# and 17#), indicating insignificant magnesium incorporated in the anodic film. This result is inconsistent with reports in the literature indicating that magnesium species migrate through the film to enter the electrolyte [15–16]. A cavity is present above the single particle in Fig. 2(c), and the EDS results show that this type of

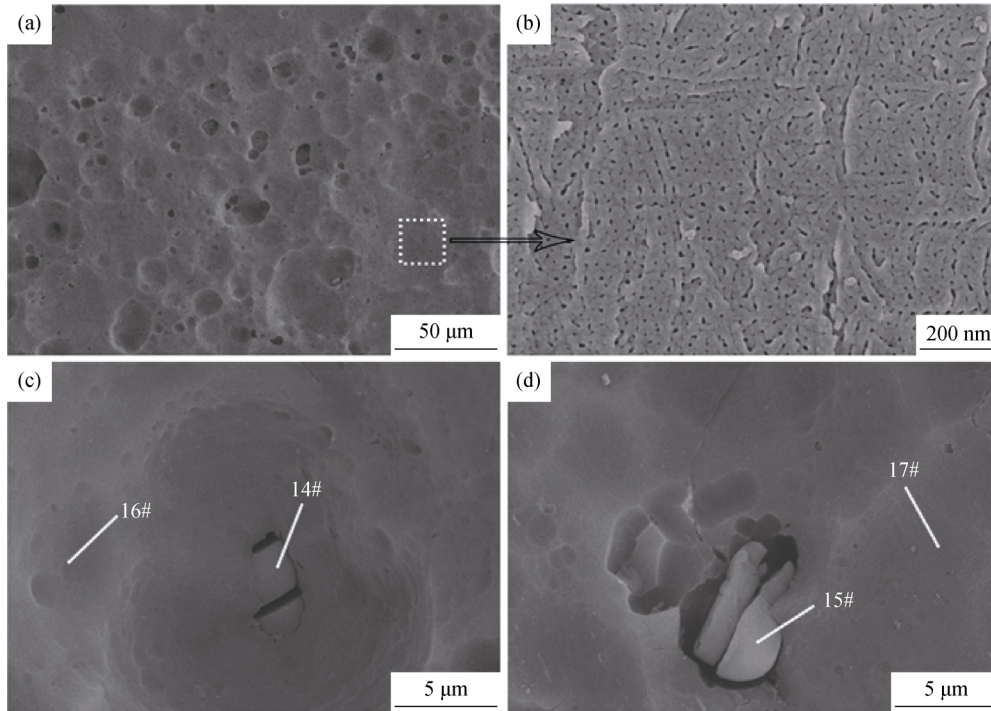


Fig. 2. SEM micrographs of 5A06 aluminum alloy after anodizing: (a) overall morphology; (b) local amplified area; (c) particles within the film; (d) particles on the film surface.

Table 1. Chemical composition of intermetallics and substrate after etching and desmutting in Fig. 1 and after anodizing in Fig. 2 determined by EDS

Points	Fe	Mn	Mg	Si	O	Al
1#	6.73	5.54	0.99	—	—	86.74
2#	5.98	3.74	3.64	—	—	86.63
3#	6.74	3.89	2.61	—	—	86.76
4#	7.36	4.37	2.06	—	—	86.20
5#	2.07	1.65	6.11	—	2.11	88.06
6#	2.15	1.40	6.37	—	—	88.21
7#	2.17	1.61	6.05	—	—	88.17
8#	—	—	7.32	—	0.99	91.69
9#	—	—	7.37	—	0.78	91.86
10#	—	2.22	6.85	—	—	90.94
11#	—	0.50	7.17	—	3.32	89.00
12#	—	1.74	6.91	—	1.27	90.07
13#	—	0.76	7.34	—	—	91.90
14#	—	—	—	31.24	60.21	8.55
15#	—	—	—	25.47	63.41	11.13
16#	—	—	—	—	50.50	49.50
17#	—	—	—	—	55.95	44.05

particle is enriched in silicon. Generally, silicon exists as a solid solution or a second-phase material in the 5A06 aluminum alloy matrix. During anodizing, active magnesium is dissolved preferentially from Mg_2Si intermetallics because the work function for pure Si in vacuum conditions (4.85 eV) is higher than those of Mg (3.66 eV) and Al (4.19 eV) [17]. Therefore, silicon is expected to be enriched within the alloy immediately beneath the thickening anodic film. When a critical enrichment is attained, silicon is gradually oxidized with surrounding aluminum [18]. As a consequence, the ordinary growth of pores is terminated above silicon-enriched particles. Meanwhile, the types of cavities (size and shape) always depend on the particle morphology. Figs. 2(c) and (d) suggest that silicon-containing particles (both as intermetallics and individual elements) are occluded in porous anodic alumina during the initial anodizing. With further anodizing, the alloy/film interface gradually recedes, and new silicon-containing particles are encountered. However, the aluminum matrix adjacent to the particles recedes more rapidly, leaving gaps between individual particles, as shown in Fig. 2(c). Subsequently, alumina around silicon-contain-

ing particles is rapidly encroached due to the presence of partially-anodized silicon particles within the anodic film. Clearly, only fine particles are readily occluded in the oxide, whereas coarse particles tend to detach from the film.

The TEM images of the anodic film cross-section demonstrate the influence of intermetallics during the anodizing process. Fig. 3(a) shows the relatively regular porous structure of the anodic film; the pore diameter is nearly 10 nm, in accordance with SEM observations. The micrograph reveals that these pores are perpendicular to the alloy substrate, and that the barrier layer locates at the base of pores (Fig. 3(c)). No magnesium enrichment is observed beneath the anodic film due to the lower Gibbs free energy per equivalent for the formation of MgO relative to that of Al_2O_3 [15–16]. The barrier layer, which exhibits a scalloped appearance between the film and the alloy substrate, has a thickness of about 16.5 nm and demonstrates a barrier layer formation ratio close to $1.1 \text{ nm}\cdot\text{V}^{-1}$ at an applied anodizing voltage of 15 V. This is consistent with the range of barrier layer thickness ($1.0\text{--}1.4 \text{ nm}\cdot\text{V}^{-1}$) previously reported for a similar anodizing voltage and several acid anodizing baths [19].

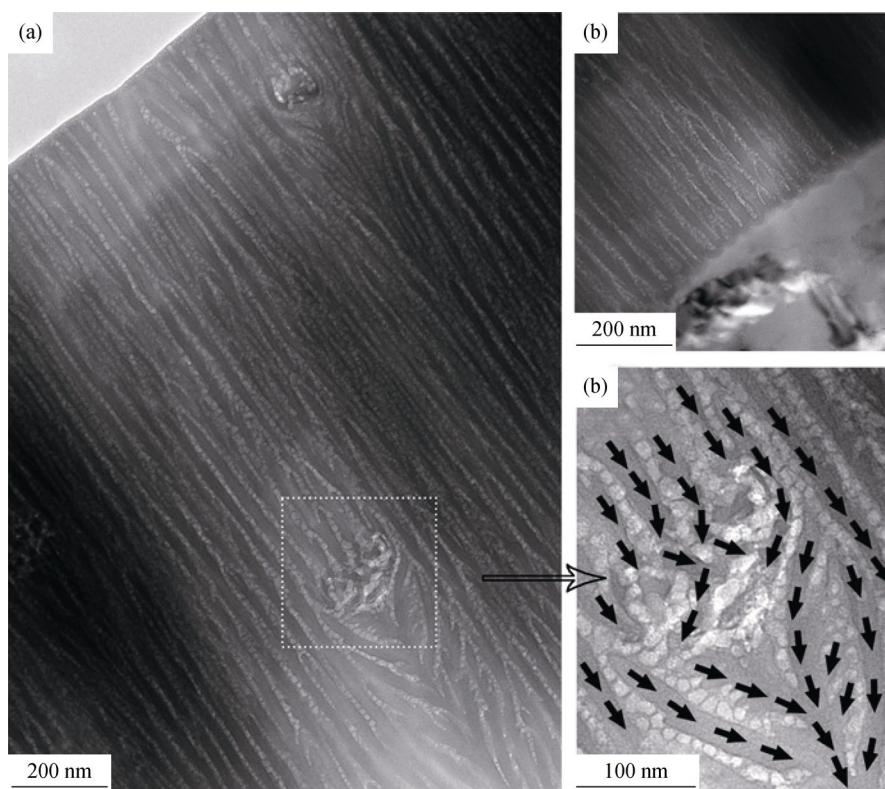


Fig. 3. TEM micrographs of the cross-section of the anodic film (a), the film/substrate interface (b), and the local distorted area indicated by black arrows (c).

Fig. 3(a) also reveals that several sites are decorated by volute features. The growth direction of regular pores seems to be distorted, and the complex porosity develops beneath

these sites. However, careful scrutiny of this special area (Fig. 3(c)) reveals the absence of substantial particles; only aluminum and oxygen are detected by EDS analysis. Sili-

con-containing particles have been reported to always maintain their original shape during anodizing due to the formation of a barrier-type SiO_2 anodic film [18]. Thus, the dissolved particle is most likely related to Al–Fe–Mg–Mn intermetallic compounds. Black arrows in Fig. 3(c) help demonstrate the growth direction of pores. Initially, metallic ions migrate from the alloy surface to the electrolyte, while the anodic film develops in the opposite direction. Subsequently, intermetallics are gradually dissolved, leaving voids in their places. Simultaneously, aluminum from both the separation of the second phase and the matrix is gradually anodized to fill these voids. As a consequence, the formed alumina displays irregular features with pore branching and deflection. Additionally, the dissolution process also makes the oxidation proceed at a reduced rate with respect to the aluminum matrix, leading to the disordering of porous anodic alumina under intermetallics. The regular amorphous film develops only at positions without intermetallic particles.

In summary, the barrier layer initially forms at the electrolyte/substrate interface and then gradually develops towards the alloy matrix. The effects of intermetallic phases on the anodic film growth can be described by two processes shown in Fig. 4. One refers to Al–Fe–Mg–Mn intermetallic phases, which tend to dissolve and distort the growth direction of pores. The film formation process under these intermetallics is also influenced. The other schematic refers to silicon-containing intermetallic phases. During anodizing, this type of intermetallic phase almost maintains its original shape. However, the adjacent alloy substrate around this type of particle is preferentially dissolved, leaving substantial gaps between the alumina and the individual particle. After anodizing, silicon-containing particles are observed to be embedded in separate cavities within the film.

3.3. Electrochemical behavior of the anodized film

As described above, intermetallics greatly influenced the film formation process. Defects were created from either the detachment of silicon-containing phases or the irregular arrangement of pores by the dissolution of Al–Fe–Mg–Mn intermetallics. Hence, the protective property of the anodic film was influenced accordingly. Fig. 5 shows the Bode diagram measured at open circuit potential (E_{ocp}) for different immersion times in a 3.5wt% NaCl solution. In a general way, a $R(\text{QR})(\text{QR})$ model proposed in Fig. 5 is used to fit the spectra to further illustrate the protective mechanism of the anodic film during immersion. In this model, R_s is the electrolytic resistance, C_p and R_p describe the capacitance

and resistance of the porous layer, respectively, and C_b and R_b are the capacitance and resistance provided by the barrier layer, respectively.

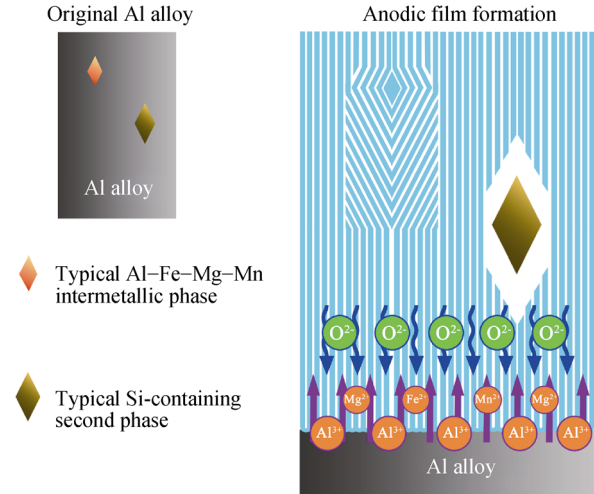


Fig. 4. Effect of intermetallic phases on the anodic film growth process.

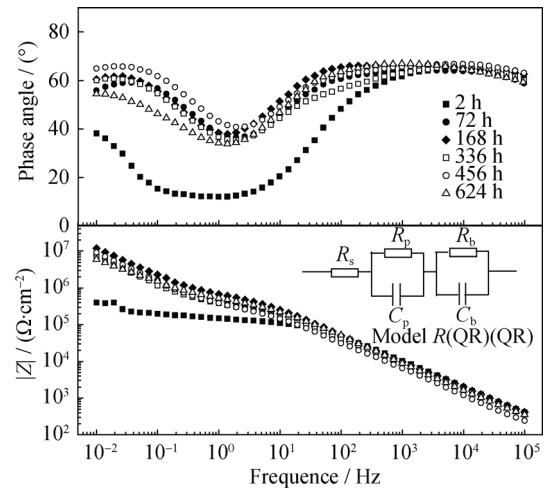


Fig. 5. Bode plots obtained in a 3.5wt% NaCl solution for sealed anodic films immersed for different times with an equivalent circuit used for fitting.

The phase angle spectrum demonstrates well-defined maxima in the low- and high-frequency ranges, corresponding to two time constants of the anodic film. The low-frequency maximum relates to the barrier layer. After 72 h of immersion, a remarkable increase in phase angle is observed, indicating major changes in barrier layer properties. In contrast, the high-frequency maximum is associated with the porous layer. During immersion, no obvious changes are observed, revealing the considerable stability of the porous layer. The impedance spectra show that the impedance values in the low frequency range significantly increase by two orders of magnitudes from 10^5 to $10^7 \Omega \cdot \text{cm}^2$.

This indicates that the major changes in barrier layer properties are associated with the improved corrosion resistance, indicating a self-sealing capacity. Similar results have also been reported by several other researchers [20–21].

For the $R(QR)(QR)$ model, a constant phase element (CPE) is employed to demonstrate the heterogeneities of the filmed samples in particular. Due to the non-ideal capacitive behavior of simple capacitances, the CPE is superior to simple capacitances (C) by $CPE = 1/C(i\omega)^\alpha$, where i stands for the imaginary unit, ω the angular frequency, and α the frequency dispersion factor. The parameter α varies from 1 to 0, C is considered as the real capacitance only when $\alpha = 1$. The model parameters are simulated and listed in Table 2 with respect to the equivalent circuit. Fig. 6 shows the evolution of resistances (R_p and R_b) and capacitances (C_p and C_b) as a function of immersion time. As shown in Fig. 6(a), the R_b values are almost two orders of magnitude higher than R_p , indicating that the corrosion resistance provided by the barrier layer is dominant. During immersion, the parameters associated with the porous layer (R_p and C_p) remain almost unchanged. However, the immersion process is always accompanied by the penetration of the surrounding electrolyte. The porous layer stability suggests that the penetration may

be completed at the very beginning of immersion. This result is related to the cavities and the loose arrangement of pores generated by different types of intermetallics within the porous layer. In contrast, the values of R_b gradually increase with immersion time, suggesting an improvement in barrier layer resistance. Fig. 6(b) also shows that after 72 h of immersion, C_b decreases by almost one order of magnitude from 10^{-5} to 10^{-6} $F\cdot cm^{-2}$. Generally, C_b is associated with the parameters of ϵ_0 , ϵ , S and d , which represent the dielectric constant in vacuum, the relative constant for aluminum oxide, the electrode surface area, and the barrier layer thickness, respectively; these parameters are related by $C_b = \epsilon_0\epsilon S/d$. Therefore, the decrease in C_b is related to the increase in d and/or the decrease in ϵ [22]. Pitting corrosion has been reported to develop preferentially along the interface between the anodic film and the substrate [23–24]. As the main second phase in the substrate, the $\beta(Al_3Mg_2)$ phase acts as the cathode site and prefers to dissolve in aggressive environments, even though the barrier layer is integral. However, the presence of an anodic film, especially the barrier layer, limits the diffusion of products, leading to the accumulation of oxides or hydroxides in a very limited local area. This explains why the dielectric properties of the

Table 2. Fitting parameters of the Bode plots in Fig. 5.

Time / h	$R_p / (k\Omega\cdot cm^2)$	CPE(P)		$R_b / (k\Omega\cdot cm^2)$	CPE(B)	
		$C_p / (\mu F\cdot cm^{-2})$	α_p		$C_b / (\mu F\cdot cm^{-2})$	α_b
2	138.6	0.1554	0.7328	1.949×10^4	15.58	0.6098
72	341.7	0.2485	0.6894	2.440×10^4	1.104	0.8096
168	648.1	0.2079	0.7123	5.044×10^4	0.768	0.8242
336	282.8	0.2674	0.7013	3.771×10^4	1.263	0.7862
456	273.2	0.3279	0.7172	5.522×10^4	1.018	0.8232
624	330.7	0.1736	0.7818	1.648×10^4	1.051	0.6544

Note: CPE(P) and CPE(B) represent CPE for the porous layer and barrier layer, respectively, and α_p and α_b represent the frequency dispersion factor for the porous layer and barrier layer, respectively.

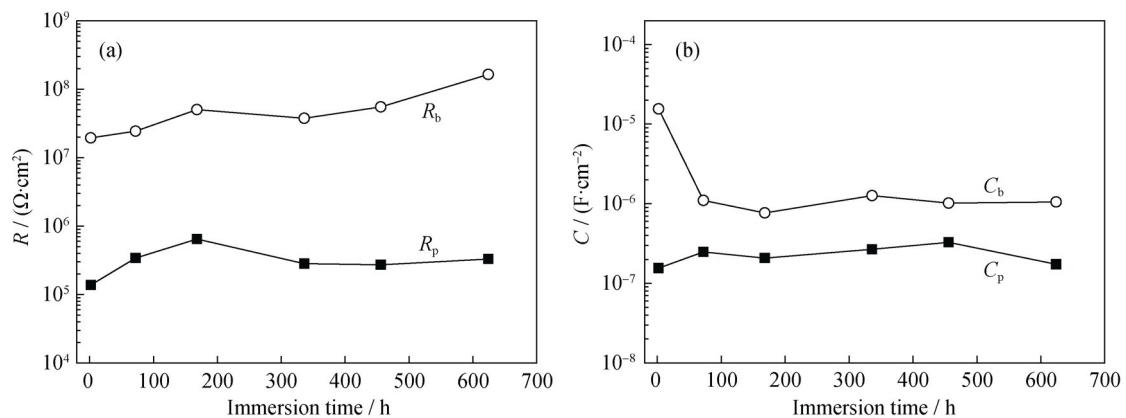


Fig. 6. Evolution of the resistance (a) and capacitance (b) of the porous layer and barrier layer during immersion.

barrier layer change during immersion. Yasakau *et al.* [8] found that the decreased magnesium content was accompanied by the appearance of an oxygen peak, resulting from the formation of oxide or hydroxide compounds. The hydroxide deposits could then form an additional diffusion barrier, hindering the further propagation of localized corrosion attacks. Obviously, the variation in C_b requires a period of induction time, and the initial 2 h of immersion is not sufficient to complete the entire process.

The corrosion resistance of the anodic film is further illustrated by Tafel polarization curves, as shown in Fig. 7. Generally, corrosion potential (E_{corr}) and corrosion current density (j_{corr}) are used to evaluate the protective properties of anodic films; these are calculated by Tafel extrapolation from the linear polarization region. The potential biasing on the anodic and cathodic branches is carried out in a small range (generally 25–100 mV) to give the Tafel slope of the linear j - E relation near E_{corr} . Linear extrapolation to E_{corr} then gives the corresponding j value (j_{corr}) [25].

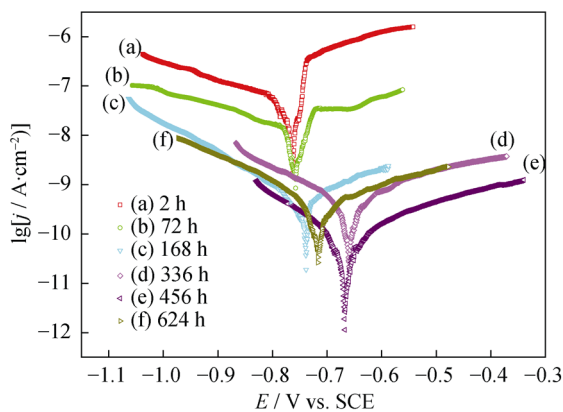


Fig. 7. Tafel polarization curves of sealed anodic films immersed in a 3.5wt% NaCl solution for different times.

Table 3 lists the parameters of anodic slope (b_{anodic}), j_{corr} , and E_{corr} for the anodized specimens derived from the polarization curves. The values of j_{corr} decrease by almost three orders of magnitude from the initial value of 106 nA cm^{-2} to 0.184 nA cm^{-2} after 456 h of immersion. Meanwhile, the values of E_{corr} increase from -0.765 V to -0.665 V. These results also demonstrate the self-healing behavior mentioned previously. The decrease in j_{corr} is likely associated with the enhancement of the barrier layer, and the changes in the dielectric properties of the barrier layer can also explain the self-healing behavior of the entire anodic film. After 624 h of immersion, the values of j_{corr} increase slightly, while E_{corr} decreases to -0.719 V. This may be associated with the breakdown of the barrier layer in the aggressive environment.

Table 3. Data for the sealed anodic films extracted from the Tafel plots in Fig. 7.

Immersion time / h	$E_{\text{corr}} / \text{V}$	$j_{\text{corr}} / (\text{nA}\cdot\text{cm}^{-2})$	$b_{\text{anodic}} / (\text{V}\cdot\text{dec}^{-1})$
2	-0.765	106	0.538
72	-0.756	24.1	0.387
168	-0.738	1.12	0.398
336	-0.656	1.06	0.529
456	-0.665	0.184	0.390
624	-0.719	0.423	0.317

4. Conclusions

(1) After pretreatment, the main residual particles are Al-Fe-Mg-Mn intermetallics, and the particle size gradually decreases with iron content from several microns to submicron-range.

(2) After anodizing, the amount of intermetallics decreases significantly, and the main residual particles are silicon-containing phases. The anodic film develops towards the alloy substrate, and the presence of intermetallics gives rise to the development of complex porosity in the anodic film beneath the dissolved intermetallics.

(3) The formed porous layer is easily penetrated, and the barrier plays a dominant role in the overall protection. Meanwhile, the self-healing behavior is observed during the immersion process due to the improvement in barrier layer properties.

Acknowledgements

This work was financially supported by the National Natural Science Foundation of China (No.51271012).

Open Access This article is distributed under the terms of the Creative Commons Attribution License which permits any use, distribution, and reproduction in any medium, provided the original author(s) and the source are credited.

References

- [1] R. Kaibyshev, F. Musin, D.R. Lesuer, and T.G. Nieh, Superplastic behavior of an Al-Mg alloy at elevated temperatures, *Mater. Sci. Eng. A*, 342(2003), No. 1-2, p. 169.
- [2] R. Goswami, G. Spanos, P.S. Pao, and R.L. Holtz, Precipitation behavior of the β phase in Al-5083, *Mater. Sci. Eng. A*, 527(2010), No. 4-5, p. 1089.
- [3] G. Lucadamo, N.Y.C. Yang, C.S. Marchi, and E.J. Lavernia, Microstructure characterization in cryomilled Al 5083, *Mater. Sci. Eng. A*, 430(2006), No. 1-2, p. 230.

- [4] Y. Yoon and R.G. Buchheit, Dissolution behavior of Al₂CuMg (S phase) in chloride and chromate conversion coating solutions, *J. Electrochem. Soc.*, 153(2006), No. 5, p. B151.
- [5] R.H. Jones, D.R. Baer, M.J. Danielson, and J.S. Vetrano, Role of Mg in the stress corrosion cracking of an Al–Mg alloy, *Metall. Mater. Trans. A*, 32(2001), No. 7, p. 1699.
- [6] K. Mizuno, A. Nylund, and I. Olefjord, Surface reactions during pickling of an aluminium-magnesium-silicon alloy in phosphoric acid, *Corros. Sci.*, 43(2001), No. 2, p. 381.
- [7] V. Guillaumin and G. Mankowski, Localized corrosion of 2024 T351 aluminium alloy in chloride media, *Corros. Sci.*, 41(1998), No. 3, p. 421.
- [8] K.A. Yasakau, M.L. Zheludkevich, S.V. Lamaka, and M.G.S. Ferreira, Role of intermetallic phases in localized corrosion of AA5083, *Electrochim. Acta*, 52(2007), No. 27, p. 7651.
- [9] R.G. Buchheit, R.P. Grant, P.F. Hlava, B. Mckenzie, and G.L. Zender, Local dissolution phenomena associated with S phase (Al₂CuMg) particles in aluminum alloy 2024–T3, *J. Electrochem. Soc.*, 144(1997), No. 8, p. 2621.
- [10] X. Zhou, G.E. Thompson, P. Skeldon, G.C. Wood, K. Shimizu, and H. Habazaki, Anodic oxidation of an Al–2 wt% Cu alloy: effect of grain orientation, *Corros. Sci.*, 41(1999), No. 6, p. 1089.
- [11] M.A. Páez, T.M. Foong, C.T. Ni, G.E. Thompson, K. Shimizu, H. Habazaki, P. Skeldon, and G. Wood, Barrier-type anodic film formation on an Al–3.5 wt% Cu alloy, *Corros. Sci.*, 38(1996), No. 1, p. 59.
- [12] L. Iglesias-Rubianes, S. Garcia-Vergara, P. Skeldon, G.E. Thompson, J. Ferguson, and M. Beneke, Cyclic oxidation processes during anodizing of Al–Cu alloys, *Electrochim. Acta*, 52(2007), No. 24, p. 7148.
- [13] J.H. Liu, M. Li, S.M. Li, and M. Huang, Effect of the microstructure of Al 7050–T7451 on anodic oxide formation in sulfuric acid, *Int. J. Miner. Metall. Mater.*, 16(2009), No. 4, p. 432.
- [14] A. Aballe, M. Bethencourt, F.J. Botana, J. Cano, and M. Marcos, EIS study of the electrochemical response of AA5083 alloy under anodic polarisation, *Corros. Rev.*, 18(2000), No. 1, p. 1.
- [15] Y. Liu, P. Skeldon, G.E. Thompson, H. Habazaki, and K. Shimizu, Anodic film growth on an Al–21at.%Mg alloy, *Corros. Sci.*, 44(2002), No. 5, p. 1133.
- [16] R.O. Mota, Y. Liu, O.R. Mattos, P. Skeldon, and G.E. Thompson, Influences of ion migration and electric field on the layered anodic films on Al–Mg alloys, *Corros. Sci.*, 50(2008), No. 5, p. 1391.
- [17] J.A. Dean, *Lange's Handbook of Chemistry*, 15th ed., McGraw-Hill Book Company, New York, 1999, p. 938.
- [18] L.E. Fratila-Apachitei, F.D. Tichelaar, G.E. Thompson, H. Terry, P. Skeldon, J. Duszczyk, and L. Katgerman, A transmission electron microscopy study of hard anodic oxide layers on AlSi (Cu) alloys, *Electrochim. Acta*, 49(2004), No. 19, p. 3169.
- [19] M. García-Rubio, M.P. de Lara, P. Ocón, S. Diekhoff, M. Beneke, A. Lavía, and I. García, Effect of posttreatment on the corrosion behaviour of tartaric–sulphuric anodic films, *Electrochim. Acta*, 54(2009), No. 21, p. 4789.
- [20] S. Feliu Jr., J.A. González, V. López, M.J. Bartolome, E. Escudero, and E. Otero, Characterisation of porous and barrier layers of anodic oxides on different aluminium alloys, *J. Appl. Electrochem.*, 37(2007), No. 9, p. 1027.
- [21] M.G. Hosseini, M. Raghbi-Boroujeni, I. Ahadzadeh, R. Najjar, and M.S. Seyed Dorraji, Effect of polypyrrole–montmorillonite nanocomposites powder addition on corrosion performance of epoxy coatings on Al 5000, *Prog. Org. Coat.*, 66(2009), No. 3, p. 321.
- [22] V. Moutarlier, M.P. Gigandet, J. Pagetti, and L. Ricq, Molybdate/sulfuric acid anodising of 2024-aluminium alloy: influence of inhibitor concentration on film growth and on corrosion resistance, *Surf. Coat. Technol.*, 173(2003), No. 1, p. 87.
- [23] V. Moutarlier, M.P. Gigandet, and J. Pagetti, Characterisation of pitting corrosion in sealed anodic films formed in sulphuric, sulphuric/molybdate and chromic media, *Appl. Surf. Sci.*, 206(2003), No. 1-4, p. 237.
- [24] J.J. Ren and Y. Zuo, Study of electrochemical behavior and morphology of pitting on anodized 2024 aluminum alloy, *Surf. Coat. Technol.*, 182(2004), No. 2-3, p. 237.
- [25] G. Wranglén, *An Introduction to Corrosion and Protection of Metals*, Springer, Berlin, 1985, p.